Ab Initio All-Electron Periodic Hartree−Fock Study of Hydrostatic Compression of Pentaerythritol Tetranitrate

Holmann V. Brand*

MS T085, Applied Physics Division, Los Alamos National Laboratory, Los Alamos, New Mexico 87545

Received: March 1, 2005; In Final Form: May 2, 2005

We present a computational study of hydrostatic compression effects on the pentaerythritol tetranitrate (PETN) energetic material up to 22.7 GPa by means of the ab initio all-electron periodic Hartree−Fock quantum mechanical method with the STO-3G Gaussian basis set. We fitted the calculated volume−energy relation to the energy SJEOS polynomial function from which we obtained the compression dependence of the pressure (P), the bulk modulus (B), and its pressure derivative (B'). We also fitted the experimental volume−pressure relation to the pressure SJEOS polynomial function, which allowed us to calculate the experimental bulk modulus (B_{exp}) and its pressure derivative (B'_{exp}). Our calculated values, $B = 6.73$ GPa and $B' = 24.63$, are in reasonable agreement with the values $B_{exp} = 8.48$ GPa and $B'_{exp} = 14.42$ from our fit to the experimental X-ray data and with the value $B_{exp} = 9.8$ GPa that was derived from the experimental elastic constants. In addition, we present a discussion on how the lattice vectors and the internal coordinates (i.e., bond lengths, bond angles, and torsion angles) of the $C(CH_2ONO_2)_4$ molecules in the PETN lattice change during hydrostatic compression of the crystal. Our calculated results suggest that the $C(CH_2ONO_2)_4$ molecules cannot be considered as being rigid but are in fact flexible, accommodating lattice compression through torsions, bendings in their bond angles, and contractions in their bond lengths. At pressures higher than about 8 GPa, however, both the $C(CH_2ONO_2)_4$ molecules and the c lattice vector seem to stiffen somewhat. The a lattice vector does not exhibit this stiffening. As a consequence, the pressure dependence of the c/a ratio shows a minimum at about 8 GPa.

I. Introduction

Typical energetic materials are hydrogen-bonded molecular crystals that release enormous amounts of chemical energy when mechanically or electrically shocked.[1−3] Pentaerythritol tetranitrate, also known as PETN, is an important energetic material[4−9] whose shock sensitivity has a fascinating crystal orientation dependence.[10,11] Two crystal phases of PETN are known. The first phase is stable at ambient conditions,[4−7] whereas the second phase occurs at higher temperatures.[8] Because the chemical reactions by which energetic materials release energy involve the breakage and formation of chemical bonds, their investigation calls for a computational method based on quantum mechanics. Quantum mechanical studies of molecules that form these energetic molecular crystals have been straightforwardly carried out for many isolated molecules in the gas phase.[3,12−15] However, only a few quantum mechanical investigations have considered the solid-phase nature of energetic molecular crystals.[16−18] This is due to the high computational cost of solid-phase calculations involving the relatively large number of atoms in the unit cell of a typical energetic molecular crystal.

The ab initio all-electron Hartree−Fock quantum mechanical computational method with the STO-3G Gaussian basis set[19] has been used extensively in the calculation of molecular geometries at relatively modest computational cost.[19−22] Recently, the periodic implementation of this method,[23] hereafter denoted HF/STO-3G, has also proven to be useful in the calculation of geometrical parameters in solids.[24−27] Hence, our interest is in documenting the ability of HF/STO-3G to predict the lattice changes of the ambient crystal phase of PETN under hydrostatic compression. The ambient crystal phase of PETN is a particularly interesting energetic material to study with a quantum mechanical computational method, because it has a relatively small unit cell with only two $H_8C_5N_4O_{12}$ molecules per unit cell, and the compression-induced changes in its lattice have been measured.[7] At ambient conditions, PETN is arranged in a tetragonal lattice (i.e., $a_0 = b_0 \neq c_0$ and $\alpha = \beta = \gamma = 90°$) with space group $P\bar{4}2_1c$ (Figure 1) and volume $V_0 = a_0^2c_0$. Each of the two $H_8C_5N_4O_{12}$ molecules in this lattice has a $C(CH_2ONO_2)_4$ conformation such that the four CH_2ONO_2 branches are related with S_4 point group symmetry. In addition, both molecules have the same internal coordinates (i.e., the same

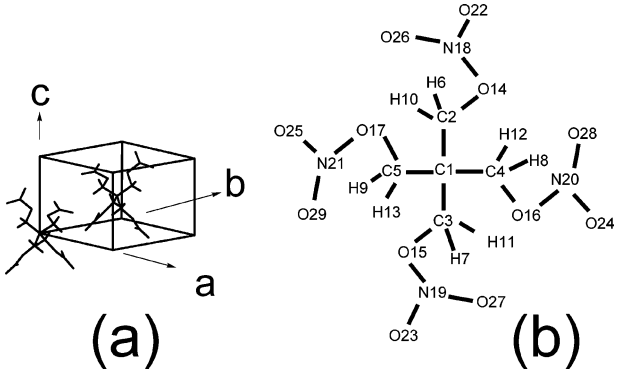

Figure 1. (a) Unit cell and lattice vectors of PETN with its two $C(CH_2ONO_2)_4$ molecules. (b) Schematic of $C(CH_2ONO_2)_4$ molecule defining atom labels used in this study.

* brand@lanl.gov.

10.1021/jp051045v
Published on Web 06/24/2005

bond lengths and angles) differing only in location and orientation in the unit cell. The first molecule is centered at fractional coordinates 0, 0, 0, whereas the second molecule is centered at fractional coordinates $^1/_2$, $^1/_2$, $^1/_2$.

In this paper, we report the performance of the HF/STO-3G quantum mechanical method with regard to the hydrostatic compression of the ambient crystalline phase of PETN. The remainder of this manuscript is organized as follows: In the second section, we describe the computational method, the third section describes the results, and finally, the fourth section lists the main conclusions of the present work.

II. Computational Method

We calculated the ground-state energy of the ambient crystal phase of PETN by means of the HF/STO-3G method as implemented in the CRYSTAL03 software.[28,29] A detailed explanation of the operation of CRYSTAL03 has been provided by Pisani et al.[23] In our calculations, the self-consistent-field procedure was converged to less than 10^{-7} au in energy. Tolerances for the Coulomb and exchange series were 10^{-6}. These tolerance settings are either equivalent to or better than those used previously.[25−27] The initial geometry for the PETN lattice was taken from the experimental structure of ref 6, which contains locations of the H atoms. Convergence of the ground-state energy of the crystal with respect to *k*-point meshing was tested at the experimental geometry by calculating the energy with an increasing number of *k* points until the energy did not change with the addition of more *k* points. The smallest *k*-point mesh needed for a converged value of the energy was used in all subsequent calculations. Since compressing the direct lattice tends to expand the reciprocal lattice, we also verified that the *k* point convergence at the experimental equilibrium volume still remained valid when the experimental equilibrium volume was isotropically compressed by 30%.

We considered a set of compressed and expanded volumes $V_i = a_i^2 c_i$ where $a_i = a_0(\delta_i)^{1/3}$ and $c_i = c_0(\delta_i)^{1/3}$ with δ_i ranging from 0.6699 to 1.0527. The optimal c_i^*/a_i^* ratio that minimized the energy at each volume V_i was found by varying the c_i/a_i ratio according to the volume-preserving variations $a_i/\sqrt{\epsilon}$ and $c_i\epsilon$ where ϵ ranged from 0.9 to 1.1 in steps of 0.02 while $\epsilon \leq 0.98$ or $\epsilon \geq 1.02$ and in steps of 0.01 or smaller while in the $0.98 < \epsilon < 1.02$ range. At each a_i/c_i ratio considered, the position of the atoms was optimized by an automated gradient-based procedure that preserved the space group symmetry of the unit cell while keeping the lattice vectors a_i and c_i constant in magnitude and direction. This automatic procedure was set to stop when the energy gradient was less than or equal to 10^{-6} in magnitude.[28] All the geometry optimizations of atoms were started with the same fractional coordinates. At each volume V_i, we fit a polynomial to the pairs of c_i/a_i ratio value and its corresponding energy E_i, from which we obtained the optimal c_i^*/a_i^* ratio with minimum energy E_i^* at each volume V_i. Then, having obtained the minimum energy E_i^* at each volume V_i, we fitted the pairs of E_i^* and V_i values to the energy SJEOS function, described below, and used the fitted function to obtain the calculated equilibrium volume at which the energy was minimal.

Since our calculated volume−energy relation was fit to the theoretically motivated energy SJEOS polynomial function,[30] we now include a brief description of the SJEOS polynomial functions for the sake of completeness. Accordingly, we make use of the dimensionless compression factor *x*, defined as

$$x = \left(\frac{V}{V_0}\right)^{1/3} \tag{1}$$

where V is the volume per unit cell and V_0 is its experimental equilibrium volume. Then, the energy E of the unit cell, the pressure P, the bulk modulus B, and the pressure derivative of the bulk modulus B' can be related as

$$P(x) = -\frac{dE}{dV} = -\frac{1}{3V_0x^2}\frac{dE}{dx} \tag{2}$$

$$B(x) = -V\frac{dP}{dV} = -\frac{x}{3}\frac{dP}{dx} \tag{3}$$

$$B'(x) = \frac{dB}{dP} = -\frac{x}{3}\frac{1}{B}\frac{dB}{dx} \tag{4}$$

Following ref 30, we write the energy E of the unit cell in terms of $^1/_x$ as the energy SJEOS polynomial

$$E(x) = \frac{a_3}{x^3} + \frac{a_2}{x^2} + \frac{a_1}{x} + a_0 \tag{5}$$

from which, according to eqs 2−4, the SJEOS expression for pressure, bulk modulus, and first derivative of the bulk modulus follow

$$P(x) = \frac{1}{3V_0}\left(\frac{3a_3}{x^6} + \frac{2a_2}{x^5} + \frac{a_1}{x^4}\right) \tag{6}$$

$$B(x) = \frac{1}{9V_0}\left(\frac{18a_3}{x^6} + \frac{10a_2}{x^5} + \frac{4a_1}{x^4}\right) \tag{7}$$

$$B'(x) = \frac{54a_3x^{-6} + 25a_2x^{-5} + 8a_1x^{-4}}{27a_3x^{-6} + 15a_2x^{-5} + 6a_1x^{-4}} \tag{8}$$

It is encouraging that Alchagirov et al.[30] and Teter et al.[31] found that fitting the calculated volume dependence of the energy to eq 5 was better than fitting to other functions such as those of Murnaghan[32] and Birch.[33,34]

For consistent comparison with experiment, we also fitted the volume dependence of the experimental pressure P_{exp} reported in ref 7 to the pressure SJEOS function conveniently written as

$$P_{exp}(x) = \frac{b_6}{x^6} + \frac{b_5}{x^5} + \frac{b_4}{x^4} \tag{9}$$

from which, according to eqs 3 and 4, the following expressions for the experimental bulk modulus B_{exp} and its pressure derivative B'_{exp} follow

$$B_{exp}(x) = \frac{1}{3}\left(\frac{6b_6}{x^6} + \frac{5b_5}{x^5} + \frac{4b_4}{x^4}\right) \tag{10}$$

$$B'_{exp}(x) = \frac{36b_6x^{-6} + 25b_5x^{-5} + 16b_4x^{-4}}{18b_6x^{-6} + 15b_5x^{-5} + 12b_4x^{-4}} \tag{11}$$

All parameter fitting in eqs 5 and 9 and function minimizations were carried out with the MATHEMATICA software.[35]

III. Results

The *k*-point dependence of the HF/STO-3G energy at the experimental geometry is listed in Table 1.

TABLE 1: Dependence of Energy on *k*-point Mesh at Experimental Equilibrium Volume and at a Compressed Volume[a]

	HF/STO-3G	
k-point mesh	$V_0 = a_0^2 c_0$	$(0.7)V_0 = [(0.7)^{1/3}a_0]^2[(0.7)^{1/3}c_0]$
$2 \times 2 \times 2$	−2583.9287677	−2580.5835018
$4 \times 4 \times 4$	−2583.9287678	−2580.5835024
$8 \times 8 \times 8$	−2583.9287678	−2580.5835024
$12 \times 12 \times 12$	−2583.9287678	−2580.5835024

[a] Energy in hartree. The experimental fractional coordinates of the ambient structure were used in the compressed volume calculation.

Evidently, the HF/STO-3G energy is converged with the $4 \times 4 \times 4$ *k*-point mesh as compared with the larger and more expensive $8 \times 8 \times 8$ and $12 \times 12 \times 12$ *k*-point meshes. Interestingly, the HF/STO-3G energy remained converged with the $4 \times 4 \times 4$ *k*-point mesh even when the experimental lattice was isotropically compressed by 30%. Therefore, all subsequent calculations in this work were done with the $4 \times 4 \times 4$ *k*-point mesh.

The energy profiles at each expanded or compressed volume V_i as a function of the volume-preserving deformation parameter ϵ are shown in Figure 2. For ease of comparison, the minimum of the energy profile at each volume V_i was set to zero in Figure 2. These energy profiles are shallower at the less compressed volumes and become steeper at the more compressed volumes. Furthermore, the energy values at $\epsilon = 0.9$ and $\epsilon = 1.1$ are comparable at volumes near V_0 but are drastically different at the most compressed volumes where the energy at $\epsilon = 0.9$ is much higher than that at $\epsilon = 1.1$. Since the volume-preserving deformations were $a_i/\sqrt{\epsilon}$ and $c_i\epsilon$, higher energies at $\epsilon = 0.9$ than at $\epsilon = 1.1$ imply that the PETN lattice, when very compressed, energetically opposes volume-preserving deformations that result in a smaller *c*/*a* ratio more strongly than volume-preserving deformations that result in a larger *c*/*a* ratio. Hence, Figure 2 reveals that, at the most compressed volumes, the PETN lattice is drastically less compressible along the *c* axis than along the *a* axis. The calculated volume−energy relation (i.e., the V_i/V_0, E_i^* pairs) was fitted to the energy SJEOS function (eq 5), from which the minimum-energy volume (the calculated equilibrium volume) was obtained. The calculated lattice vectors *a* and *c* of this minimum-energy volume are listed in Table 2 along with the experimental values.[6−8] Our calculated lattice vectors *a* and *c* at the equilibrium volume are shorter than the experimental values by about 0.13 and 0.02 Å, respectively. This is likely due to the fact that the HF/STO-3G method, as observed in molecular calculations,[19] underestimates distances involved in hydrogen bonding. By comparison, the calculated lattice vectors from the Γ-point density functional theory (DFT) study of ref 18 were longer than experiment by about 0.05 Å. The pair of lattice vectors a_i^* and c_i^* that minimized the energy at each volume V_i is listed in Table 3 along with the corresponding minimum energy E_i^*. The energy corresponding to the equilibrium volume was arbitrarily set to zero in Table 3, and all other energies were specified in kilocalories per mole with respect to this zero energy value. Using the SJEOS coefficients from the fit and eqs 6−8, we obtained, for each V_i/V_0, the corresponding calculated pressure *P*, bulk modulus *B*, and pressure derivative of the bulk modulus d*B*/d*P*. These are listed in Table 3.

Figure 3a shows the V_i/V_0, E_i^* pairs as empty circles and the energy SJEOS fit as a solid line. The pressure SJEOS relation (eq 6), with coefficients from the energy SJEOS fit, is shown as a solid line in Figure 3b. The filled circles in Figure 3b are the experimental V_i/V_0, *P* values of ref 7. The dotted line is the pressure SJEOS function (eq 9) fitted to these experimental volume−pressure values. As shown in Figure 3b, the calculated pressure appears slightly below the experimental data (filled circles). However, since the calculated equilibrium volume is smaller than the experimental equilibrium volume V_0 of ref 7 by a factor of 0.967 159, shifting the calculated pressure curve to the right by a factor of $1 - 0.967\,159$ would actually show that the calculated pressure (empty circles) is slightly above the experimental data (filled circles). Hence, the calculated PETN lattice is in reality slightly stiffer than the experimental data.

Figure 4a shows the calculated bulk modulus *B* versus pressure, listed in Table 3, as a solid line. Figure 4a also shows the experimental bulk modulus versus pressure B_{exp}, obtained from eq 10, as a dotted line. Evidently, for most pressures, *B* is above B_{exp}, suggesting that the calculated PETN lattice is slightly stiffer than experiment. Although *B* is smaller than B_{exp} at zero pressure, it quickly becomes larger than B_{exp} at low pressure. This is consistent with Figure 4b, which shows that the pressure derivative of the calculated bulk modulus B' (solid line) is much larger than that of the experimental bulk modulus B'_{exp} (dotted line) at low pressure and then only slightly larger with increasing pressure. Our calculated values, $B = 6.73$ GPa and $B' = 24.63$, at the calculated equilibrium geometry are in reasonable agreement with the values $B_{exp} = 8.48$ GPa and $B'_{exp} = 14.42$ that we derived from the pressure SJEOS function (eq 9) fitted to the experimental data of ref 7 and evaluated at the experimental geometry V_0. We also note that another estimate for B_{exp} at zero pressure can be obtained from the experimental elastic constants C_{ij} from ref 36 and the relation[37]

$$B_{exp} = \frac{C_{33}(C_{11} + C_{12}) - 2C_{13}^2}{C_{11} + C_{12} + 2C_{33} - 4C_{13}} \tag{12}$$

which gives 9.8 GPa. This independent B_{exp} value compares well with the 8.48 GPa value obtained from the pressure SJEOS function fitted to the volume−pressure data of ref 7. Hence, our calculated bulk modulus (6.73 GPa) is smaller than both experimental estimates. Nevertheless, it is encouraging that our calculated bulk modulus (6.73 GPa) based on the HF/STO-3G method is closer to the experimental estimates (8.48−9.8 GPa) than the calculated value (14.5−16.0 GPa) predicted by the Γ-point DFT study of ref 18.

Figure 5 shows the compression-induced changes in the lattice vectors *a* and *c*, as well as their *c*/*a* ratio. The evolution of the lattice vectors *a* and *c* with increasing pressure is listed in Table 3 and shown in Figure 5a,b as empty circles. The corresponding experimental values of *a* and *c*, from ref 7, are shown as filled circles for comparison. The calculated *a* vector underestimates the experimental values especially at lower pressure, but agreement improves with increasing pressure. On the other hand, the calculated *c* vector slightly overestimates the experimental values at most pressures. The pressure dependence of the *c*/*a* ratio is shown in Figure 5c. The calculated *c*/*a* ratio overestimates the experimental values at all pressures considered and shows a spurious peak at ∼0.6 GPa, a decrease to a minimum at ∼8 GPa, and an increase at higher pressures. The minimum at ∼8 GPa in the calculated *c*/*a* ratio is related to the fact that the pressure dependence of the calculated *c* vector suddenly changes to a less steep slope at ∼8 GPa (i.e., the *c* vector becomes less compressible at ∼8 GPa), whereas the calculated *a* vector changes slope only gradually with increasing pressure. Consistent with this minimum in our calculated *c*/*a* ratio, the

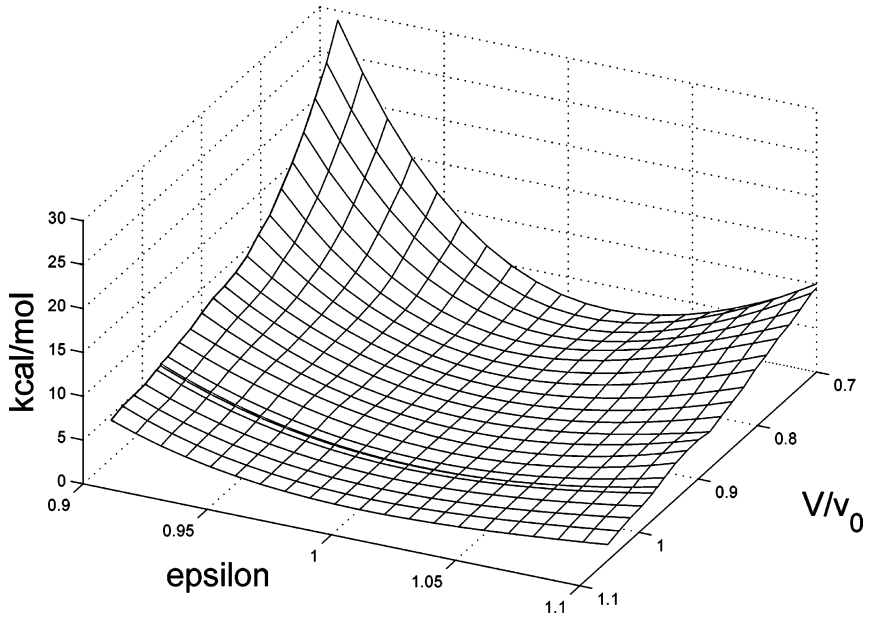

Figure 2. Energy profile at each V/V_0 as a function of the volume-preserving deformation parameter ϵ. The minimum of each energy curve was set to zero for ease of comparison.

TABLE 2: Calculated and Experimental Lattice Parameters of PETN[a]

	calculated	experiment		
lattice variable	HF/STO-3G	ref 6	ref 7	ref 8
a_0	9.25061	9.3776	9.383	9.38
c_0	6.67771	6.7075	6.711	6.71
$V_0 = a_0^2 c_0$	571.43692	589.8534	590.841	590.38

[a] Lattice vectors a_0 and c_0 in angstroms. Lattice volume V_0 in cubic angstroms.

Γ-point DFT study of ref 18 also found a minimum in the calculated c/a ratio at ∼7 GPa. Although the experimental c/a ratio data from ref 7 shown in Figure 5c is noisy, it does seem to decrease as the pressure increases to ∼5 GPa. At pressures above ∼5 GPa, the scatter in the experimental data is even noisier, but the c/a ratio seems to stop decreasing. As a last comment to Figure 5c, we note that the fact that our calculated c vector appears to be generally more compressible than the a vector at pressures below ∼8 GPa and less compressible than the a vector at higher pressures is consistent the experimental finding[36] that, for PETN at zero pressure, the elastic constant C_{33} is smaller than the elastic constant C_{11}. In addition, the softer lattice vector c can also be expected to be more thermally expandable than the stiffer lattice vector a. As reported in ref 38 for PETN at ambient conditions, the thermal coefficient of the lattice vector c is in fact larger than that of the lattice vector a.

In the discussion below, we will comment on the particular manner in which the $C(CH_2ONO_2)_4$ molecules accommodate hydrostatic compression under the constraints imposed by the PETN lattice and will attempt to correlate the behavior of their internal coordinates (bond lengths and angles) with that of the lattice vectors a and c. For the sake of clarity, all unique internal coordinates of the $C(CH_2ONO_2)_4$ molecules are grouped and numbered in Table 4 according to the atom labels shown in Figure 1b. For example, the eight CH bonds of each $C(CH_2ONO_2)_4$ molecule are grouped in the two unique internal coordinates 2 and 3 (see Table 4) corresponding to CH(2) and CH(3). Similarly, the eight NO bonds of the NO_2 moieties in each molecule are grouped in the two unique internal coordinates

TABLE 3: Compression Dependence of Calculated Quantities[a]

V/V_0	a (Å)	c (Å)	energy (kcal/mol)	pressure (GPa)	bulk modulus (GPa)	dB/dP
0.66990	8.1589	5.9359	156.9332	22.67	148.42	4.71
0.68904	8.2555	5.9635	124.2452	18.76	129.63	4.90
0.70818	8.3411	6.0040	97.6926	15.44	113.03	5.11
0.72732	8.4299	6.0371	75.9280	12.63	98.34	5.34
0.74646	8.5209	6.0643	58.2579	10.24	85.31	5.61
0.76560	8.6007	6.1050	43.9826	8.23	73.74	5.91
0.78474	8.6612	6.1704	32.6977	6.54	63.45	6.27
0.80388	8.7264	6.2268	23.7113	5.12	54.29	6.69
0.82302	8.7809	6.2962	16.8407	3.94	46.12	7.19
0.84216	8.8385	6.3589	11.4751	2.97	38.84	7.79
0.86130	8.8998	6.4142	7.4748	2.17	32.33	8.55
0.88044	8.9682	6.4570	4.5280	1.52	26.52	9.52
0.89958	9.0184	6.5242	2.4610	1.01	21.33	10.81
0.91872	9.0663	6.5927	1.1041	0.61	16.69	12.62
0.93786	9.1325	6.6328	0.3355	0.31	12.53	15.34
0.95700	9.2092	6.6559	0.0326	0.10	8.82	19.90
0.96878	9.2506	6.6777	0.0000	0.00	6.73	24.63
0.96944	9.2552	6.6757	0.0199			
0.97614	9.2831	6.6815	0.0961			
0.99528	9.3519	6.7125	0.2099			
1.01442	9.4113	6.7556	0.3551			
1.03356	9.4777	6.7869	0.7248			
1.05270	9.5240	6.8456	1.2678			

[a] The calculated pressure P, bulk modulus B, and pressure derivative of the bulk modulus dB/dP were obtained from eqs 2.6−2.8 using parameters from the energy SJEOS function (eq 2.5) fitted to the calculated volume-energy relation.

6 and 7 that correspond to NO(6) and NO(7). In the discussion that follows, however, these bond lengths will be referred to as simply CH and NO, unless making a specific distinction is necessary.

Compression-induced changes in the internal coordinates of the $C(CH_2ONO_2)_4$ molecules are listed in Tables 5−7 and displayed in Figures 6−8. In general, the calculated equilibrium values (zero pressure) of the internal coordinates are in reasonable agreement with experiment. The calculated equilibrium bond lengths tend to be only slightly longer than experiment. The calculated equilibrium angles agree with experiment within 3°. The calculated equilibrium torsion angles

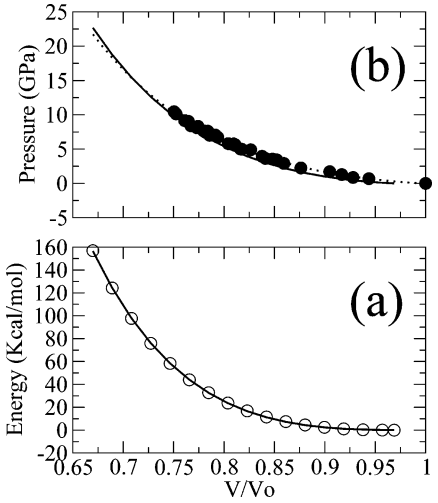

Figure 3. (a) V/V_0 dependence of energy. Calculated values in open circles. Solid line is the energy SJEOS function (eq 5) fitted to the calculated volume−energy relation. (b) V/V_0 dependence of pressure. Experimental values in filled circles. The dashed line is the pressure SJEOS function (eq 9) fitted to the experimental volume−pressure data. The solid line is the calculated pressure (eq 6) using the parameters from the energy SJEOS function that was fitted to the calculated volume−energy relation.

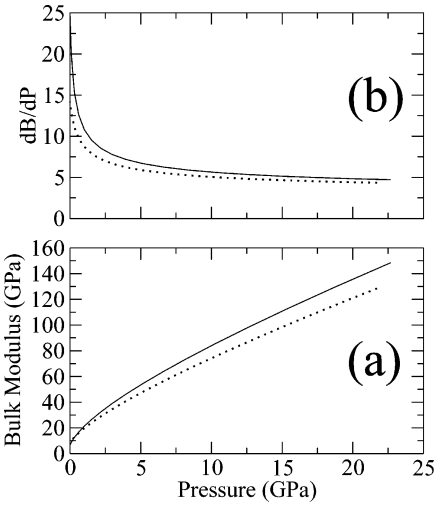

Figure 4. (a) Pressure dependence of the bulk modulus. The solid line is the calculated bulk modulus (eq 7) using the parameters from the energy SJEOS function fitted to the calculated volume−energy relation. The dashed line is the experimental bulk modulus (eq 10) using the parameters from the pressure SJEOS function that was fitted to the experimental volume−pressure data. (b) Pressure dependence of the pressure derivative of the bulk modulus. The solid line is the calculated derivative (eq 8) using the parameters from the energy SJEOS function that was fitted to the calculated volume−energy relation. The dashed line is the experimental derivative (eq 11) using the parameters from the pressure SJEOS function that was fitted to the experimental volume−pressure data.

agree well with experiment, slightly deviating by 3° in the case of CONO torsions and by 4° in the case of CCON torsions. Figures 6−8 show the calculated compression-induced changes in all internal coordinates with respect to their calculated equilibrium values. Interestingly, as we will note in the discussion below, the internal coordinates vary slightly more rapidly (somewhat steeper slopes) with increasing pressure at pressures below ∼8 GPa than at pressures above ∼8 GPa. Therefore, pressure-induced changes in the internal coordinates will indicate that the $C(CH_2ONO_2)_4$ molecules are really more flexible at pressures below ∼8 GPa than at pressures above

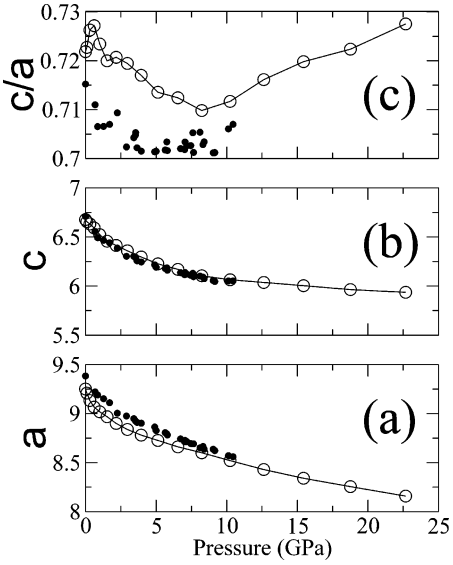

Figure 5. Pressure dependence of lattice vectors. Open circles are calculated values. Filled circles are experimental values. Circles are connected by straight lines as a visual aid. (a) Lattice vector *a*. (b) Lattice vector *c*. (c) *c*/*a* ratio. Vector magnitudes in angstroms.

TABLE 4: Definition of Internal Coordinates of $C(CH_2ONO_2)_4$ Molecules in PETN Lattice[a]

coordinate number	parameter
1	C_1C_2, C_1C_3, C_1C_4, C_1C_5
2	C_2H_6, C_3H_7,C_4H_8, C_5H_9
3	C_2H_{10}, C_3H_{11}, C_4H_{12}, C_5H_{13}
4	C_2O_{14}, C_3O_{15}, C_4O_{16}, C_5O_{17}
5	$O_{14}N_{18}$, $O_{15}N_{19}$, $O_{16}N_{20}$, $O_{17}N_{21}$
6	$N_{18}O_{22}$, $N_{19}O_{23}$, $N_{20}O_{24}$, $N_{21}O_{25}$
7	$N_{18}O_{26}$, $N_{19}O_{27}$, $N_{20}O_{28}$, $N_{21}O_{29}$
8	$C_2C_1C_3$, $C_4C_1C_5$
9	$C_2C_1C_4$, $C_2C_1C_5$, $C_3C_1C_4$, $C_3C_1C_5$
10	$C_1C_2H_6$, $C_1C_3H_7$, $C_1C_4H_8$, $C_1C_5H_9$
11	$C_1C_2H_{10}$, $C_1C_3H_{11}$, $C_1C_4H_{12}$, $C_1C_5H_{13}$
12	$C_1C_2O_{14}$, $C_1C_3O_{15}$, $C_1C_4O_{16}$, $C_1C_5O_{17}$
13	$H_6C_2H_{10}$, $H_7C_3H_{11}$, $H_8C_4H_{12}$, $H_9C_5H_{13}$
14	$H_6C_2O_{14}$, $H_7C_3O_{15}$, $H_8C_4O_{16}$, $H_9C_5O_{17}$
15	$C_2O_{14}N_{18}$, $C_3O_{15}N_{19}$, $C_4O_{16}N_{20}$, $C_5O_{17}N_{21}$
16	$O_{14}N_{18}O_{22}$, $O_{15}N_{19}O_{23}$, $O_{16}N_{20}O_{24}$, $O_{17}N_{21}O_{25}$
17	$O_{14}N_{18}O_{26}$, $O_{15}N_{19}O_{27}$, $O_{16}N_{20}O_{28}$, $O_{17}N_{21}O_{29}$
18	$O_{22}N_{18}O_{26}$, $O_{23}N_{19}O_{27}$, $O_{24}N_{20}O_{28}$, $O_{25}N_{21}O_{29}$
19	$C_3C_1C_2H_6$, $C_2C_1C_3H_7$, $-C_5C_1C_4H_8$, $-C_4C_1C_5H_9$
20	$C_3C_1C_2H_{10}$, $C_2C_1C_3H_{11}$, $-C_5C_1C_4H_{12}$, $-C_4C_1C_5H_{13}$
21	$C_3C_1C_2O_{14}$, $C_2C_1C_3O_{15}$, $-C_5C_1C_4O_{16}$, $-C_4C_1C_5O_{17}$
22	$C_1C_2O_{14}N_{18}$, $C_1C_3O_{15}N_{19}$, $-C_1C_4O_{16}N_{20}$, $-C_1C_5O_{17}N_{21}$
23	$C_2O_{14}N_{18}O_{22}$, $C_3O_{15}N_{19}O_{23}$, $-C_4O_{16}N_{20}O_{24}$, $-C_5O_{17}N_{21}O_{25}$
24	$C_2O_{14}N_{18}O_{26}$, $C_3O_{15}N_{19}O_{27}$, $-C_4O_{16}N_{20}O_{28}$, $-C_5O_{17}N_{21}O_{29}$

[a] Atom labels defined according to Figure 1b.

∼8 GPa. Despite this slight flexibility loss, we will clearly see that, in the entire pressure range considered in this study (up to ∼22.7 GPa), the $C(CH_2ONO_2)_4$ molecules cannot be considered as being rigid. This is in sharp contradiction with the results of the Γ-point DFT study of hydrostatic compression of PETN in ref 18, which concluded that the $C(CH_2ONO_2)_4$ molecules were rigid up to a pressure of ∼7 GPa and then exhibited very abrupt changes in their internal coordinates at higher pressures. This radical difference may be due to the fact that, besides numerical effects related to electron correlation and basis sets, the validity of the Γ-point approximation used in ref 18 is questionable, particularly at compressed volumes.

TABLE 5: Pressure Dependence of Bond Lengths (internal coordinates 1−7) of the $C(CH_2ONO_2)_4$ Molecules in the PETN Lattice[a]

	bond length (Å)						
pressure (GPa)	1	2	3	4	5	6	7
22.67	1.5094	1.0815	1.0816	1.4467	1.4011	1.2606	1.2658
18.76	1.5159	1.0837	1.0837	1.4480	1.4050	1.2619	1.2666
15.44	1.5218	1.0855	1.0857	1.4492	1.4085	1.2632	1.2672
12.63	1.5273	1.0871	1.0873	1.4501	1.4117	1.2642	1.2678
10.24	1.5322	1.0885	1.0887	1.4511	1.4144	1.2652	1.2683
8.23	1.5366	1.0897	1.0899	1.4519	1.4170	1.2660	1.2687
6.54	1.5406	1.0906	1.0909	1.4525	1.4191	1.2669	1.2690
5.12	1.5439	1.0915	1.0917	1.4531	1.4210	1.2675	1.2693
3.94	1.5469	1.0922	1.0925	1.4536	1.4227	1.2681	1.2696
2.97	1.5495	1.0928	1.0930	1.4540	1.4243	1.2685	1.2698
2.17	1.5517	1.0933	1.0935	1.4542	1.4256	1.2689	1.2699
1.52	1.5534	1.0937	1.0939	1.4544	1.4266	1.2693	1.2700
1.01	1.5549	1.0940	1.0942	1.4545	1.4275	1.2695	1.2701
0.61	1.5561	1.0943	1.0944	1.4546	1.4282	1.2698	1.2702
0.31	1.5571	1.0945	1.0946	1.4547	1.4288	1.2699	1.2702
0.10	1.5578	1.0947	1.0947	1.4546	1.4294	1.2700	1.2702
0.00	1.5581	1.0947	1.0948	1.4545	1.4296	1.2702	1.2701
exptl	1.5298	0.9880	0.9656	1.4460	1.4032	1.1985	1.1925

[a] Internal coordinates defined as in Table 4. Experimental values from ref 6.

Changes in calculated bond lengths (i.e., internal coordinates 1−7) due to hydrostatic compression are listed in Table 5. Compression-induced variations from their calculated equilibrium values are shown in Figure 6. Clearly, Figure 6 shows that hydrostatic compression causes all bond lengths of the $C(CH_2ONO_2)_4$ molecules to shorten. The CC bonds are the most affected by compression, becoming ∼0.05 Å shorter at the largest pressure considered here (22.76 GPa). The ON bonds are also sensitive, becoming ∼0.03 Å shorter at 22.76 GPa. However, the CH, CO, and NO bonds were not as sensitive to compression, decreasing in length by only ∼0.01 Å or less. Nevertheless, it is worth mentioning that both of the two CH bonds decrease by the same amount, whereas the two NO bonds of each NO_2 moiety decrease by slightly different amounts. We also note the gradual change in slope (see Figure 6) in the compression-dependent decrease of the CC and ON bond lengths at ∼8 GPa. This slope change suggests that the CC and NO bonds become slightly less compressible at pressures above ∼8 GPa.

Table 6 lists the calculated bond angles (i.e., internal coordinates 8−18) as a function of pressure. Figure 7 shows the changes from their equilibrium values. Figure 7 shows that, upon compression, the ONO(17), CCO, CON, and CCC(8) bond angles decrease, while the CCC(9), CCH(11), ONO(16), HCH(13), and ONO(18) bond angles increase. The largest change upon compression is seen in the 3.5° and 3.7° decrease of the CON and CCC(8) bond angles, respectively, at the highest pressure. The CON bond angle becomes slightly less compressible at ∼8 GPa, as evidenced by a slight change in slope at ∼8 GPa. The CCC(8) bond angle appears to have changes in slope at ∼8 and ∼15 GPa. The ONO(17) and CCO bond angles, however, continue to decrease without any perceptible change in slope with increasing pressure. At pressures below ∼8 GPa, the CCH(11) bond angle shows the fastest increase, while the CCC(9) bond angle increases slightly less. But at pressures above ∼8 GPa, this pattern is reversed with the CCH(11) bond angle increasing less rapidly than the CCC(9) bond angle. Similarly, at pressures below ∼8 GPa, the CCH(10) bond angle slightly increases, while the HCO(14) bond angle slightly decreases. At pressures above ∼8 GPa, the CCH(10) bond angle no longer increases and starts to slightly decrease, while the HCO(14) bond angle stops decreasing and begins to slightly increase. The ONO(16) bond angle, on the other hand, shows no change in rate of increase as the pressure increases.

Table 7 lists the calculated torsion (dihedral) angles (i.e., internal coordinates 19−24) as a function of pressure. Changes in these coordinates from their calculated zero-pressure values are shown in Figure 8. Fascinatingly, Figure 8 shows concerted motion in the CONO and CCCH torsion (dihedral) angles by about the same amount but in different directions. This suggests that the compression-induced torsions of the NO_2 and CH_2 moieties are correlated. This pattern is consistent with the fact that the inter- and intramolecular hydrogen bonding among the $C(CH_2ONO_2)_4$ molecules occurs between the NO_2 and CH_2 moieties. In addition, we note that the fact that the CCON torsion angle, which defines the spatial location of the NO_2 moieties, is the most affected by compression thus indicating that the $C(CH_2ONO_2)_4$ molecules respond to hydrostatic compression by rotating the location of the NO_2 moieties about their CO axis. We also note the gradual slope change in the compression-induced changes of all torsion angles at ∼8 GPa. The only experimental attempt to measure compression-induced changes in the torsion angles of PETN was complicated by the fact that the samples were deuterated.[39] The compression behavior of the lattice vectors of the deuterated PETN samples was significantly different from that of the regular protonated samples,[7] thus suggesting different compression effects in the deuterated molecules that are beyond the scope of the present work. Nevertheless, we point out that the experimental study of ref 39 found the $C(CD_2ONO_2)_4$ molecules in the deuterated PETN samples to be flexible at pressures up to 4.28 GPa.

From the above discussion of Tables 5−7 and Figures 6−8, it is clear that the $C(CH_2ONO_2)_4$ molecules lose some flexibility at pressures above ∼8 GPa but cannot be considered rigid. We now attempt to correlate this stiffening of the $C(CH_2ONO_2)_4$ molecules that begins at ∼8 GPa with the minimum found in the pressure dependence of the *c*/*a* ratio, shown in Figure 5c, at a pressure of ∼8 GPa. First, we begin by noticing that, in the PETN lattice, the shortest distance between the central C atom of two neighboring $C(CH_2ONO_2)_4$ molecules is equal to the magnitude of the lattice vector *c* and in the direction of the lattice vector *c* (and is therefore independent of the lattice vector *a*), whereas the next-to-shortest distance between the central C atom of two $C(CH_2ONO_2)_4$ molecules is $\sqrt{a^2/2+c^2/4}$ (and therefore depends on the magnitudes of the lattice vectors *a* and *c*). To see this, let us compare the distance between the central C atom of one $C(CH_2ONO_2)_4$ molecule with Cartesian coordinates (0, 0, 0) and another molecule whose central C atom is at (0, 0, ±*c*), namely *c*, with that of the distance between the central C atom of the two $C(CH_2ONO_2)_4$ molecules in the unit cell having Cartesian coordinates (0, 0, 0) and ($^a/_2$, $^a/_2$, $^c/_2$), namely $\sqrt{a^2/2+c^2/4}$. Within the pressure range considered in this study, $\sqrt{a^2/2+c^2/4}$ is about 0.5 Å longer than *c*. Second, we point out that the space between the CH_2ONO_2 branches of one $C(CH_2ONO_2)_4$ molecule accommodate the CH_2ONO_2 branches of neighboring molecules. Hence, because of these two reasons, we propose that any flexibility loss in the $C(CH_2ONO_2)_4$ molecules will likely have an effect on the shortest distance between the central C atoms of neighboring molecules, namely the magnitude of the lattice vector *c*, more than on the next-to-shortest distance $\sqrt{a^2/2+c^2/4}$, which is about 0.5 Å longer. Therefore, the stiffening of the $C(CH_2ONO_2)_4$ molecules correlates with the stiffening of the *c*

TABLE 6: Pressure Dependence of Bond Angles (Internal coordinates 8 through 18) of the $C(CH_2ONO_2)_4$ Molecules in the PETN Lattice[a]

	bond angle (°)										
pressure (GPa)	8	9	10	11	12	13	14	15	16	17	18
22.67	107.90	110.26	110.11	111.97	105.02	109.55	110.78	106.58	113.79	117.87	128.29
18.76	108.46	109.98	110.16	111.83	105.36	109.47	110.68	106.99	113.64	118.13	128.20
15.44	108.94	109.74	110.20	111.71	105.67	109.38	110.61	107.37	113.52	118.35	128.10
12.63	109.39	109.51	110.21	111.60	105.95	109.32	110.54	107.71	113.40	118.55	128.03
10.24	109.83	109.29	110.21	111.49	106.18	109.26	110.49	108.06	113.28	118.73	127.98
8.23	110.20	109.11	110.20	111.37	106.39	109.22	110.45	108.37	113.17	118.88	127.94
6.54	110.50	108.96	110.21	111.26	106.53	109.19	110.45	108.67	113.07	119.02	127.90
5.12	110.72	108.85	110.17	111.14	106.67	109.18	110.46	108.90	113.03	119.11	127.86
3.94	110.90	108.76	110.16	111.03	106.77	109.17	110.48	109.12	112.98	119.18	127.84
2.97	111.08	108.67	110.14	110.93	106.86	109.15	110.50	109.31	112.93	119.24	127.83
2.17	111.24	108.59	110.12	110.85	106.93	109.11	110.52	109.48	112.88	119.29	127.83
1.52	111.39	108.52	110.10	110.79	106.98	109.07	110.54	109.64	112.83	119.34	127.83
1.01	111.44	108.50	110.10	110.71	106.98	109.06	110.58	109.79	112.80	119.36	127.84
0.61	111.46	108.48	110.12	110.65	106.97	109.03	110.62	109.89	112.78	119.37	127.85
0.31	111.51	108.46	110.12	110.60	106.97	108.99	110.64	109.97	112.76	119.37	127.87
0.10	111.59	108.42	110.11	110.59	106.96	108.94	110.65	110.04	112.74	119.37	127.89
0.00	111.61	108.41	110.11	110.58	106.95	108.90	110.67	110.10	112.72	119.37	127.91
exptl	112.69	107.89	111.73	112.75	106.75	106.43	109.80	113.22	112.02	117.68	130.31

[a] Internal coordinates defined as in Table 4. Experimental values from ref 6.

TABLE 7: Pressure Dependence of Torsion Angles (internal coordinates 19−24) of the $C(CH_2ONO_2)_4$ Molecules in the PETN Lattice[a]

	dihedral angle (°)					
pressure (GPa)	19	20	21	22	23	24
22.67	163.32	−74.55	44.02	162.00	183.59	1.36
18.76	163.95	−74.08	44.53	162.64	183.09	1.13
15.44	164.63	−73.56	45.11	163.47	182.34	0.66
12.63	165.37	−72.97	45.77	164.33	181.54	0.11
10.24	166.07	−72.43	46.38	165.04	180.82	−0.42
8.23	166.77	−71.86	47.02	165.81	180.02	−1.01
6.54	167.41	−71.33	47.56	166.75	179.07	−1.75
5.12	168.02	−70.83	48.09	167.70	178.14	−2.54
3.94	168.61	−70.32	48.62	168.67	177.12	−3.44
2.97	169.21	−69.83	49.15	169.56	176.27	−4.20
2.17	169.77	−69.38	49.66	170.31	175.63	−4.74
1.52	170.29	−68.98	50.13	170.87	175.16	−5.14
1.01	170.62	−68.71	50.41	171.55	174.61	−5.65
0.61	170.98	−68.42	50.72	172.31	174.14	−6.10
0.31	171.37	−68.10	51.08	172.94	173.81	−6.39
0.10	171.88	−67.67	51.59	173.13	173.78	−6.34
0.00	172.13	−67.47	51.83	173.22	173.69	−6.41
exptl	171.76	−68.42	51.71	169.44	176.78	−3.40

[a] Internal coordinates defined as in Table 4. Experimental values from ref 6.

lattice vector beginning at a pressure of ∼8 GPa by the fact that the shortest distance between the central C atoms of two $C(CH_2ONO_2)_4$ molecules is in fact the magnitude of the lattice vector *c*.

IV. Conclusions

We have presented a quantum mechanical computational study of hydrostatic compression effects on the ambient phase of crystalline PETN by means of the ab initio all-electron periodic Hartree−Fock method with the STO-3G basis set, denoted HF/STO-3G, as implemented in the CRYSTAL03 software. The volume−energy relation of the PETN lattice under hydrostatic compression was calculated by minimizing the HF/STO-3G energy at each compressed volume with respect to the position of atoms in the unit cell and volume-preserving variations in the lattice vectors. This volume−energy relation was fitted to the energy SJEOS polynomial function of ref 30. From the energy SJEOS fit, we obtained the calculated

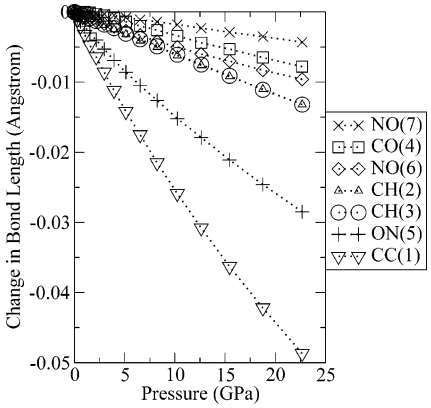

Figure 6. Calculated pressure-induced changes in the bond lengths of the $C(CH_2ONO_2)_4$ molecule relative to their calculated equilibrium values. Labels as defined in Table 4. Bond lengths in angstroms.

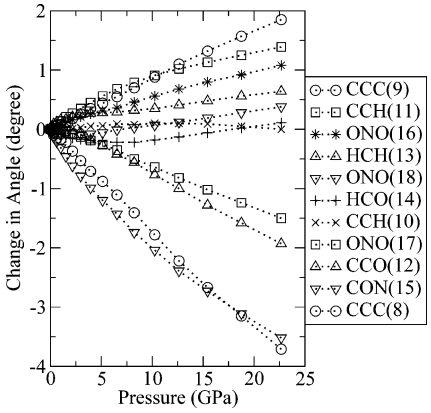

Figure 7. Calculated pressure-induced changes in the bond angles of the $C(CH_2ONO_2)_4$ molecule relative to their calculated equilibrium values. Labels as defined in Table 4. Angles in degrees.

equilibrium volume, as well as the compression dependence of the pressure, the bulk modulus *B*, and the pressure derivative of the bulk modulus *B*′. For consistent comparison with experiment, we fitted the experimental volume−pressure relation[7] with the pressure SJEOS polynomial function, which allowed us to derive the compression dependence of the experimental bulk modulus B_{exp} and its pressure derivative

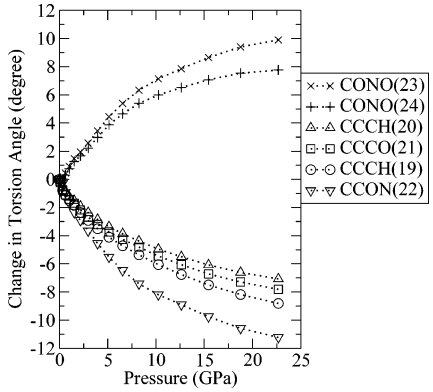

Figure 8. Calculated pressure-induced changes in the dihedral (torsion) angles of the $C(CH_2ONO_2)_4$ molecule relative to their calculated equilibrium values. Labels as defined in Table 4. Angles in degrees.

B'_{exp}. It is gratifying that our calculated zero-pressure values for the unit cell lattice vectors *a* and *c* as well as the bulk modulus *B* and its pressure derivative B' are in reasonable agreement with experiment. Our calculated values, $B = 6.73$ GPa and $B' = 24.63$, agree with the experimental values $B_{exp} = 8.48$ GPa and $B'_{exp} = 14.42$ that we derived from the pressure SJEOS function fitted to the experimental data of ref 7 and also with the value $B_{exp} = 9.8$ GPa that was derived from the elastic constants of ref 36.

We have also documented the compression-induced changes in the internal coordinates (bond lengths and angles) of the $C(CH_2ONO_2)_4$ molecules and in the lattice vectors *a* and *c*. Our results indicate that the $C(CH_2ONO_2)_4$ molecules cannot be considered as being rigid but are in fact flexible, accommodating lattice compression through torsions in their CH_2ONO_2 branches, bendings in their bond angles, and contractions in their bond lengths. At pressures higher than ~8 GPa, however, the $C(CH_2ONO_2)_4$ molecules seem to lose some flexibility as evidenced by the gradual change in slope of the pressure dependence of the internal coordinates.

Regarding the lattice, we found both lattice vectors *a* and *c* to decrease in length under hydrostatic compression, as could be expected. However, the *c* vector was surprisingly less compressible than the *a* vector at pressures above ~8 GPa, thus causing the pressure dependence of the *c*/*a* ratio to have a minimum at ~8 GPa. We found that the flexibility loss of the $C(CH_2ONO_2)_4$ molecules at ~8 GPa and the compressibility loss of the *c* lattice vector at ~8 GPa were related by the fact that in the PETN lattice the shortest distance between the central C atom of two neighboring $C(CH_2ONO_2)_4$ molecules is equal to the magnitude of the lattice vector *c*. Therefore, during compression, any stiffening of the $C(CH_2ONO_2)_4$ molecules will likely affect the *c* lattice vector. By comparison, the next-to-shortest distance between the central C atom of two $C(CH_2ONO_2)_4$ molecules corresponds to that between two molecules in the unit cell, namely $\sqrt{a^2/2+c^2/4}$, which is about 0.5 Å longer than the *c* vector, and therefore appears to be less susceptible to the stiffening of the $C(CH_2ONO_2)_4$ molecules during hydrostatic compression.

All the calculations presented here were done on a desktop computer at relatively modest computational expense. Encouraged by the performance of the HF/STO-3G method in the present calculations of PETN under hydrostatic compression, we have begun to study compression effects in other energetic materials with larger unit cells having many more atoms.

Acknowledgment. This work is supported by the U.S. Department of Energy (DOE). The author thanks Drs. J. C. Boettger, J. J. Dick, and C. W. Greeff for many helpful comments.

References and Notes

(1) Fickett, W.; Davis, W. C. *Detonation*; University of California Press: Berkeley, CA, 1979.
(2) Zukas, J. A., Walters, W. P., Eds. *Explosive Effects and Applications*; Springer-Verlag: New York, 2003.
(3) Brand, H. V.; Rabie, R. L.; Funk, D. J.; Diaz-Acosta, I.; Pulay, P.; Lippert, T. K. *J. Phys. Chem. B* **2002**, *106*, 10594, and references therein.
(4) Booth, A. D.; Llewellyn, F. J. *J. Chem. Soc.* **1947**, 837.
(5) Trotter, J. *Acta Crystallogr.* **1963**, *16*, 698.
(6) Conant, J. W.; Cady, H. H.; Ryan, R. R.; Yarnell, J. L.; Newsam, J. M. Technical Report LA-7756-MS; Los Alamos National Laboratory: Los Alamos, NM, 1979.
(7) Olinger, B.; Halleck, P. M.; Cady, H. H. *J. Chem. Phys.* **1975**, *62(11)*, 4480.
(8) Cady, H. H.; Larson, A. C. *Acta Crystallogr., Sect. B* **1975**, *31*, 1864.
(9) Winey, J. M.; Gupta, Y. M. *J. Appl. Phys.* **2001**, *90(3)*, 1669.
(10) Dick, J. J. *Appl. Phys. Lett.* **1984**, *44(9)*, 859.
(11) Dick, J. J. *J. Appl. Phys.* **1997**, *81(2)*, 601.
(12) Rice, B. M.; Hare, J. *Thermochim. Acta* **2002**, *348*, 377.
(13) Rice, B. M.; Pai, S. V.; Hare, J. *Combust. Flame* **1999**, *118*, 445.
(14) Gruzdkov, Y. A.; Gupta, Y. M. *J. Phys. Chem. A* **2001**, *105*, 6197.
(15) Chakraborty, D.; Muller, R. P.; Dasgupta, S.; Goddard, W. A. *J. Phys. Chem. A* **2001**, *105*, 1302.
(16) Kuklja, M. M.; Kunz, A. B. *J. Appl. Phys.* **2001**, *89*, 4962.
(17) Wu, C. J.; Yang, L. H.; Fried, L. E.; Quenneville, J.; Martinez, T. J. *Phys. Rev. B* **2003**, *67*, 235101.
(18) Gan, C. K.; Sewell, T. D.; Challacomb, M. *Phys. Rev. B* **2004**, *69*, 35116.
(19) Hehre, W. J.; Radom, L.; Schleyer, P. v. R.; Pople, J. A. *Ab Initio Molecular Orbital Theory*; John Wiley and Sons: New York, 1986.
(20) Brand, H. V.; Curtiss, L. A.; Iton, L. E. *J. Phys. Chem.* **1992**, *96*, 7725.
(21) Brand, H. V.; Curtiss, L. A.; Iton, L. E. *J. Phys. Chem.* **1993**, *97*, 12773.
(22) Brand, H. V.; Curtiss, L. A.; Iton, L. E. *J. Phys. Chem.* **1994**, *98*, 1293.
(23) Pisani, C.; Dovesi, R.; Roetti, C. *Hartree-Fock Ab Initio Treatment of Crystalline Systems*; Berthier, G., Ed.; Lecture Notes in Chemistry 48; Springer: Berlin, 1988.
(24) Civalleri, B.; D'Arco, Ph.; Orlando, R.; Saunders, V. R.; Dovesi, R. *Chem. Phys. Lett.* **2001**, *348*, 131.
(25) Nicholas, J. B.; Hess, A. C. *J. Am. Chem. Soc.* **1994**, *116*, 5428.
(26) White, J. C.; Nicholas, J. B.; Hess, A. C. *J. Phys. Chem. B* **1997**, *101*, 590.
(27) White, J. C.; Hess, A. C. *J. Phys. Chem.* **1993**, *97*, 8703.
(28) Saunders, V. R.; Dovesi, R.; Roetti, C.; Orlando, R.; Zicovich-Wilson, C. M.; Harrison, N. M.; Doll, K.; Civalleri, B.; Bush, I. J.; D'Arco, Ph.; Llunell, M. *CRYSTAL03 User's Manual*; University of Turin: Torino, 2003. Internet address: www.crystal.unito.it.
(29) Doll, K.; Harrison, N. M.; Saunders: V. R. *Int. J. Quantum Chem.* **2001**, *82*, 1.
(30) Alchagirov, A. B.; Perdew, J. P.; Boettger, J. C.; Albers, R. C.; Fiolhais, C. *Phys. Rev. B* **2001**, *63*, 224115.
(31) Teter, D. M.; Gibbs, G. V.; Boisen, M. B.; Allen, D. C.; Teter, M. P. *Phys. Rev. B* **1995**, *52*, 8064.
(32) Murnaghan, F. D. *Proc. Natl. Acad. Sci. U.S.A.* **1944**, *30*, 244.
(33) Birch, F. *Phys. Rev.* **1947**, *71*, 809.
(34) Birch, F. J. *Geophys. Res.* **1978**, *83*, 1275.
(35) MATHEMATICA; Wolfram Research, Champaign, IL.
(36) Winey, J. M.; Gupta, Y. M. *J. Appl. Phys.* **2001**, *90*, 1669.
(37) Morris, C. E. *Proceedings of the Sixth Symposium (International) on Detonation*; ACR-221, Office of Naval Research, Department of the Navy, Arlington, VA, 1976; p 396.
(38) Cady, H. H. *J. Chem. Eng. Data* **1972**, *17*, 369.
(39) Dick, J. J.; von Dreele, R. B. *Shock Compression of Condensed Matter*; Schmidt, Ed.; CP429; The American Institute of Physics: Woodbury, NY, 1997; p 827.